Strong and Elastic Membranes via Hydrogen Bonding Directed Self-Assembly of Atomically Precise Nanoclusters

Anirban Som, Alessandra Griffo, Indranath Chakraborty, Hendrik Hähl, Biswajit Mondal, Amrita Chakraborty, Karin Jacobs, Päivi Laaksonen, Olli Ikkala,* Thalappil Pradeep,* and Nonappa*

2D nanomaterials have provided an extraordinary palette of mechanical, electrical, optical, and catalytic properties. Ultrathin 2D nanomaterials are classically produced via exfoliation, delamination, deposition, or advanced synthesis methods using a handful of starting materials. Thus, there is a need to explore more generic avenues to expand the feasibility to the next generation 2D materials beyond atomic and molecular-level covalent networks. In this context, self-assembly of atomically precise noble nanoclusters can, in principle, suggest modular approaches for new generation 2D materials, provided that the ligand engineering allows symmetry breaking and directional internanoparticle interactions. Here the self-assembly of silver nanoclusters (NCs) capped with p-mercaptobenzoic acid ligands (Na_4Ag_{44}-$pMBA_{30}$) into large-area freestanding membranes by trapping the NCs in a transient solvent layer at air–solvent interfaces is demonstrated. The patchy distribution of ligand bundles facilitates symmetry breaking and preferential intralayer hydrogen bondings resulting in strong and elastic membranes. The membranes with Young's modulus of 14.5 ± 0.2 GPa can readily be transferred to different substrates. The assemblies allow detection of Raman active antibiotic molecules with high reproducibility without any need for substrate pretreatment.

1. Introduction

Atomically thin 2D nanomaterials have gained immense interest because of their remarkable mechanical and optoelectronic properties.[1–12] They are classically prepared using exfoliation, exploiting promoted intralayer bonding over weak interlayer interactions of their 3D counterparts.[4] The exfoliation of graphene[1] has triggered searches for other covalently interconnected atomically thin 2D nanomaterials, such as transition metal dichalcogenides,[5] Mxenes,[6] boron nitrides,[7] and clays,[8] based on exfoliation and delamination,[9] molecular beam epitaxy,[10] and advanced synthesis.[11] In ultrathin 2D nanomaterials, the quantum confinement of electrons in two dimensions opens novel applications, e.g., in flexible optoelectronic devices.[4,12,13] Beyond atomic and molecular-level networks, a less studied approach deals with the self-assembly of metal nanoparticles (NPs) to form 2D monolayer membranes, i.e., of nanometric thickness. That this could be relevant, is suggested by the tunable optoelectronic and mechanical properties of self-assembled 2D materials of narrow size dispersed plasmonic NPs.[14–17] However, metal NPs classically suffer from uncontrolled aggregation tendency, polydispersity, and lack of directional interactions.[18–21] Additionally, nonspecific bindings and slow diffusion of colloidal-level

A. Som, O. Ikkala, Nonappa
Department of Applied Physics
Aalto University
Espoo FI-02150, Finland
E-mail: olli.ikkala@aalto.fi

A. Griffo, P. Laaksonen, O. Ikkala
Department of Bioproducts and Biosystems
Aalto University
Espoo FI-02150, Finland

A. Griffo, H. Hähl, K. Jacobs
Department of Experimental Physics
Saarland University
66123 Saarbrücken, Germany

A. Griffo, K. Jacobs
Max Planck School Matter to Life
Jahnstraße 29, 69120 Heidelberg, Germany

I. Chakraborty, B. Mondal, A. Chakraborty, T. Pradeep
DST Unit of Nanoscience and Thematic Unit of Excellence
Department of Chemistry
Indian Institute of Technology Madras
Chennai 600036, India
E-mail: pradeep@iitm.ac.in

I. Chakraborty
School of Nano Science and Technology
Indian Institute of Technology
Kharagpur 721302, India

Nonappa
Faculty of Engineering and Natural Sciences
Tampere University
Tampere FI-33720, Finland
E-mail: nonappa@tuni.fi

particles could result in a mixture of different structures rather than the desired homogeneous or precise end-product.[22,23] Nevertheless, 2D close-packed arrays of gold nanoparticles, binary superlattices, and nanoparticle–polymer composite arrays have been achieved using evaporation induced assembly, interfacial assembly, binary solvents, antisolvent approach, dip coating, and Langmuir–Blodgett film formation methods.[24–27] Still, achieving a combination of precision and reproducibility of self-assembled large-area NP superstructures remains a grand challenge.[28]

Recent studies in the literature suggest that the nanoparticle size dispersity, ligand structure, and density hinders the reproducibility, sensitivity, and mechanical properties of NP-based 2D assemblies. Mueggenburg et al. have shown that NP membranes composed of dodecane thiol ligand-capped gold NPs with an average diameter of 9.4 nm show highly scattered elastic modulus with a range of 3–39 GPa.[29] The large distribution of elastic modulus is attributed to the uncertainty and compositional differences in membranes made from different nanoparticle batches. The mechanical properties of such membranes strongly depends on the ligand interdigitation and NP packing efficiency. In such systems, the core–core interactions account for less than 10% of the observed overall strength.[30] Cheng et al. used a microhole drying method to prepare DNA-capped nanoparticle membranes with inter-nanoparticle distances tunable up to 20 nm and Young's moduli within a narrow range of 6.49 ± 1.57 GPa. However, the observed average moduli values are much less than other NP membranes.[31] Gold nanoparticle-based 2D assemblies have been studied for nanoparticle–organic memory field-effect transistors.[32a] In such assemblies, the reproducibility of NP density depends on NP size and capping ligands, which in turn affect the device performances.[32a,b] Furthermore, the uniform size, density, and inter-nanoparticle distances in monolayers of plasmonic silver nanoparticles have been shown to significantly improve the surface enhanced Raman spectroscopy (SERS) sensitivity and reproducibility.[17,33–35] Therefore, there is a need to develop methods for the uniform and reproducible fabrication of precision nanoparticle assemblies.

Atomically precise, monolayer ligand-protected noble metal nanoclusters (NCs) offer tunable size, shape, composition, and oxidation states.[36] While a vast number of NCs have been synthesized over the last decade, understanding their structure, optoelectronic properties, catalysis, and biological properties remains the central theme.[36–38] NCs are excellent building blocks for well-defined assemblies, composites, and hybrid materials allowing large design flexibility and unique optoelectronic properties.[39] Therefore, the next logical step would be the creation of rationally designed assemblies of NCs to attain the desired properties. In their crystalline state, ligand–ligand interactions between the spatially arranged neighboring NCs dictate the packing geometry. Depending on the functionality, these ligands can interact through hydrogen bonding, electrostatic, dipolar, π-stacking, and van der Waals interactions.[39] The ability to manipulate such supramolecular forces in detail is the key toward controlling the geometry of the nanocluster assemblies.

Large area monolayer 2D assemblies of NCs with well-defined internal order require a restriction of the NC

crystallization in a particular direction, i.e., symmetry breaking. It has been shown using *para*-mercaptobenzoic acid (*p*MBA)-protected gold NCs (Au_{102}-*p*MBA_{44}) that symmetry breaking can be achieved by exploiting the anisotropic or patchy hydrogen bonding (H-bonding) ligand distribution.[40,41] On the other hand, atomically precise silver NCs have been utilized to achieve hydrogen bonding mediated assembly of tellurium nanowires into 2D cross-bilayer structures,[42] and selective encapsulation of plasmonic gold nanorods.[43] Liquid–liquid interfaces have also been utilized to create NC 2D assemblies.[44] However, precise control over layer thickness and structure in nanoparticle membranes covering a large area and studies on their mechanical properties is still lacking.

Here we report the fabrication of large-area (extending over cm^2) freestanding monolayer membranes of Na_4Ag_{44}-*p*MBA_{30} NCs with long-range hexagonally close-packed internal structure. The membranes are prepared by processing at air–water interfaces hosting a transient solvent layer. Specifically, we utilize the selective in-plane growth of the cluster assemblies by facilitating the intralayer H-bonding between the carboxylic acid groups of *p*MBA ligands. The packing of the NCs was analyzed using high resolution transmission electron microscopy (HR-TEM). The ultrathin membranes were also directly deposited across micrometer sized holes. The atomic force microscopy (AFM)-based force spectroscopy showed non-hysteretic elastic deformation upon nanoindentation. The observed Young's modulus of 14.5 ± 0.2 GPa, is significant for a noncovalently interconnected ultrathin membrane of colloidal units. The membranes allow detection of Raman active antibiotics dissolved in water using surface enhanced Raman spectroscopy with high reproducibility, unlike the classic nanoparticles with finite-size distributions and defected structures.

2. Results and Discussions

2.1. Microscale 2D Colloidal Crystals

We utilized atomically precise silver nanoclusters, Na_4Ag_{44}-*p*MBA_{30} (**Figure 1**a) synthesized according to a reported literature procedure (see Figure S1, Supporting Information, for details).[45,46] Formation of Na_4Ag_{44}-*p*MBA_{30} was confirmed through UV–vis spectroscopy and ESI mass spectrometry (Figure S2, Supporting Information). The solid state structure of Na_4Ag_{44}-*p*MBA_{30} consists of a 32 atom Ag core (concentric icosahedral and dodecahedral Ag atom shells), which is protected by six Ag_2-*p*MBA_5 units in an octahedral geometry (Figure 1a).

This arrangement results in the formation of *p*MBA ligand bundles or patches, which break the spherical symmetry. The ligand bundles are classified into L2 (bundle of two) and L3 (bundle of three) *p*MBA groups (Figure 1b), which act as the inter-nanocluster interaction patches to drive the 3D network formation. Incidentally, all the six L2 bundles are located along an imaginary equatorial plane and drive the crystal growth in the lateral dimension (along *ab*-plane). The six L3 bundles are placed above (three) and below (three) the equatorial plane and form H-bonded bridges between the layers (along the *c*-axis). In this way, a single
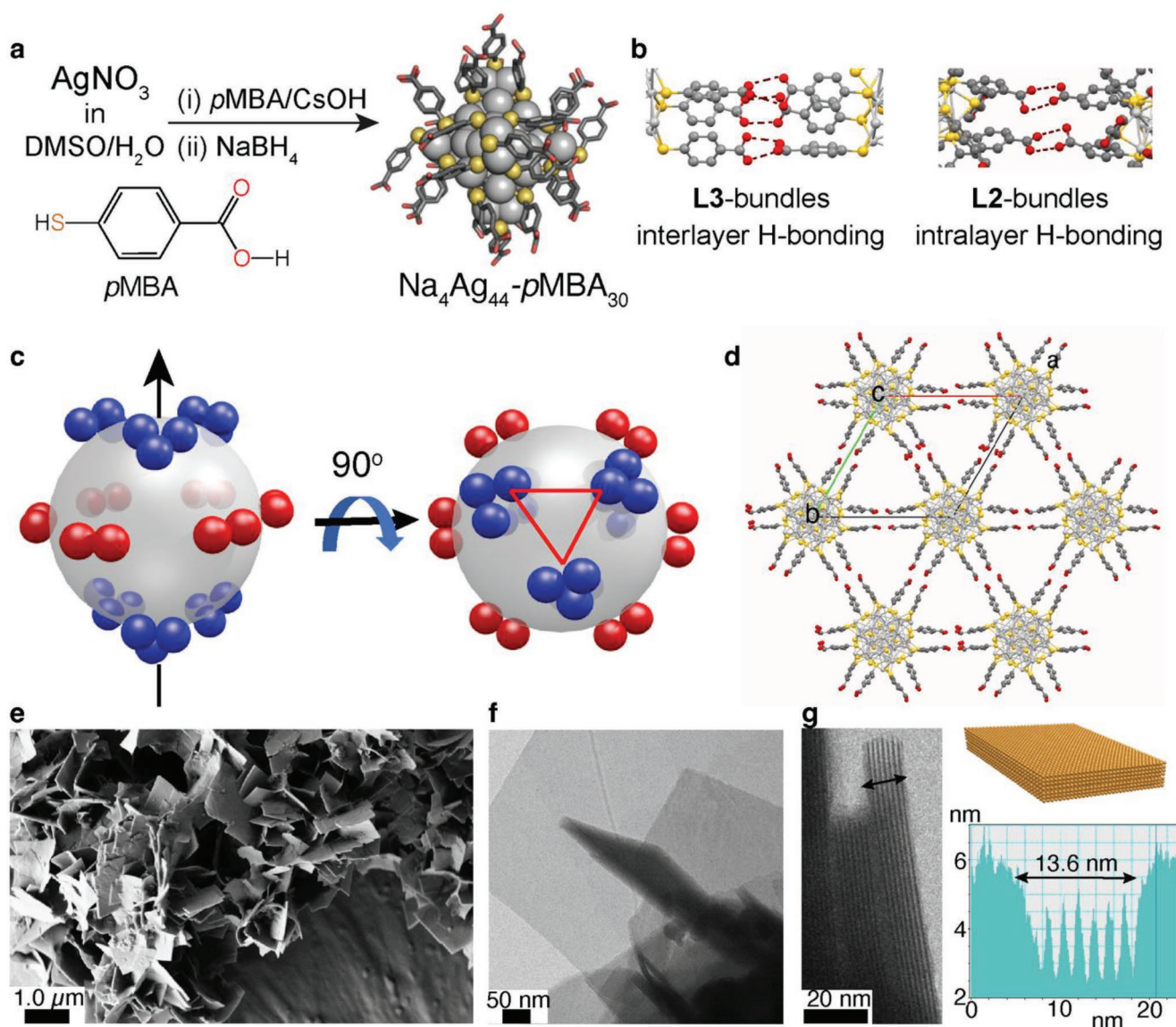
Figure 1. Synthesis, patchy ligand distribution, and 2D colloidal crystals. a) Synthesis scheme, and X-ray crystal structure of Na_4Ag_{44}-$pMBA_{30}$ (CSD entry XIMHOS, hydrogen atoms are not shown for clarity).[46] b) Representative L2 and L3 ligand bundles of Na_4Ag_{44}-$pMBA_{30}$. c) Schematic representation showing the patchy distribution of L2 (red spheres) and L3 (blue spheres) bundles. The six L2 bundles are located around an imaginary equatorial plane. d) Intralayer packing of the clusters in the crystal structure directed by L2 bundles, showing the possibility of a 2D assembly (see Figure S2d, Supporting Information, for interlayer packing via L3 bundles). e) SEM image of 2D nanosheets of Na_4Ag_{44}-$pMBA_{30}$ in methanol. f) TEM image of nanosheets. g) TEM image suggests that these nanosheets contain a few layers, as shown in the histogram.

Na_4Ag_{44}-$pMBA_{30}$ is involved in 24 H-bonds (6 × L2) with clusters from the same layer (Figure 1c). The L3 bundles contribute to 18 inter-nanocluster H-bonds each with clusters from layers above and below, respectively (Figure S2d, Supporting Information).

We envisaged that Na_4Ag_{44}-$pMBA_{30}$ provides a feasible starting point to create 2D NC superstructures (Figure 1d), as it intrinsically allows a larger number of intralayer H-bonds between the NCs compared to the interlayer bonds. The creation of 2D assemblies of Na_4Ag_{44}-$pMBA_{30}$ would thus require selectively restricting the formation of interlayer L3 H-bonds to drive the crystal growth along the lateral direction and to limit the growth in the perpendicular direction. Herein we expected that kinetically controlled self-assembly

could be feasible. To test our hypothesis, we first screened solvents to facilitate 2D colloidal crystal growth of Na_4Ag_{44}-$pMBA_{30}$, before aiming the monolayer membranes. Thus we found that, when a dispersion of Na_4Ag_{44}-$pMBA_{30}$ in N,N'-dimethylformamide (DMF) was added to methanol (nonsolvent), an immediate precipitation was observed. The scanning electron microscopy (SEM) images of the dispersion revealed the presence of microscopic 2D colloidal crystals (Figure 1e). A closer examination of TEM images revealed that these sheets are, in fact, stacks with a few layer thickness (Figure 1f). For example, in Figure 1g the TEM image shows a stack of seven layers (Figure S3c–e, Supporting Information, for HR-TEM images). Therefore, this

**ADVANCED
SCIENCE NEWS**

www.advancedsciencenews.com

**NANO · MICRO
small**

www.small-journal.com

strategy offered a certain degree of control on the 2D stacking of Na_4Ag_{44}-pMBA$_{30}$. However, precisely controlling the layer thickness and limiting it to a monolayer necessitated identifying more refined strategies.

2.2. Freestanding Monolayer Membrane

Self-assembly of molecules at interfaces (air–liquid or liquid–liquid) leading to monomolecular membranes has been investigated extensively for several decades.[47,48] Therein Langmuir–Blodgett (LB) processing allows thin membranes of a variety of nanomaterials at the air–water interface taken that they are sufficiently hydrophobic.[49] However, the Na_4Ag_{44}-pMBA$_{30}$ NCs could not be assembled using the LB-processing, as they are dispersible in water. To achieve monolayer membranes, we carried out a systematic study using a series of solvents. When a dispersion of Na_4Ag_{44}-pMBA$_{30}$ in DMF was added to ethanol, propanol, butanol, and acetone, they all resulted in mesoscale colloidal crystals similar to those in methanol (Figure S3f–i, Supporting Information). Interestingly, a stable dispersion of Na_4Ag_{44}-pMBA$_{30}$ without immediate precipitation was obtained in 1-pentanol. Exploiting this property, we first dispersed the clusters in 1-pentanol, which was subsequently transferred in a dropwise manner on a water surface (Figure S1, Supporting Information). 1-Pentanol, due to its longer alkyl chain length, has low solubility in water (22 g L^{-1}) compared to lower alcohols.

In the literature 1-pentanol has been used as a cosurfactant for stable microemulsion preparation and interface synthesis of gold mesocrystals.[50] In our experiment, when a dispersion of Na_4Ag_{44}-pMBA$_{30}$ in 1-pentanol was placed on the surface of the water, pentanol quickly spreads to form a membrane. The clusters trapped inside this pentanol layer assemble through the formation of H-bonds and float at the air–water interface (**Figure 2**a). The resulting freestanding Na_4Ag_{44}-pMBA$_{30}$ membrane can be picked from the air–water interface and transferred onto suitable substrates as shown using a glass coverslip ($d \approx 1.2$ cm). An immediate transfer of the membrane on to the substrate is better for the stability and to avoid any degradation upon contact with water for longer time. Increased concentration of 1-pentanol in water may also be detrimental for membrane preparation. For example, in a control experiment when Na_4Ag_{44}-pMBA$_{30}$ in 1-pentanol was added on the surface containing a mixture of 1-pentantol/water (2/75 v/v) resulted in droplets and no film formation was observed (Figure S1, Supporting Information).

The membranes were examined using TEM by transferring them onto TEM grids with lacey, holey, or ultrathin carbon support films. That the membrane extended over micrometer area can be seen in the large area TEM image (Figure 2b). The HR-TEM images, fast Fourier transform (FFT), and inverse fast Fourier transform (IFFT) analysis of the membrane deposited on TEM grid with ultrathin carbon support indicate the well-defined overall hexagonally close-packed (hcp) assembly as well as the membrane is of monolayer thickness (Figure 2c,d). Further analysis of the Na_4Ag_{44}-pMBA$_{30}$ monolayer membrane revealed an average interparticle distance of 2.33 nm and periodicity of 2.01 nm (Figure 2e).

The UV–vis spectrum of the Na_4Ag_{44}-pMBA$_{30}$ monolayer membranes showed the same characteristics peaks as observed for the individual solvent dispersed Na_4Ag_{44}-pMBA$_{30}$ NCs. This suggests that the intrinsic properties of the NCs are retained in the monolayer membranes (Figure 2f,g). However, the absorption peaks turned broader in the monolayer membrane, indicating a possible electronic coupling between the NCs. In the Raman spectrum, Na_4Ag_{44}-pMBA$_{30}$ monolayer membranes exhibit several peaks ranging from 300 to 1800 cm^{-1} of which two strong bands at 1077 and 1584 cm^{-1} are due to v_{12} and v_{8a} aromatic ring vibrations (of the pMBA ligands), respectively (Figure 2h; Figure S5a,b, Supporting Information). For comparison, the Raman spectrum of a drop-casted Na_4Ag_{44}-pMBA$_{30}$ film on a coverslip was taken, which shows a similar spectral pattern. Still, the peaks are better resolved in the case of Na_4Ag_{44}-pMBA$_{30}$ monolayer membranes. The most intense peak at 1584 cm^{-1} was utilized to construct the Raman spectral image (Figure S5c, Supporting Information), which resembles the optical image of the Na_4Ag_{44}-pMBA$_{30}$ monolayer membrane (Figure S5d, Supporting Information). A few regions show higher intensity (Raman spectra in Figure 2h) because of multilayers at those locations due to the folding or crumpling of Na_4Ag_{44}-pMBA$_{30}$ monolayer membranes while transferring onto the substrate.

2.3. Mechanical Properties of Na_4Ag_{44}-pMBA$_{30}$ Membranes

After a successful demonstration of the feasibility of freestanding Na_4Ag_{44}-pMBA$_{30}$ monolayer membrane formation, we turned our attention to determine the mechanical properties of the nanometric membranes. The freshly prepared Na_4Ag_{44}-pMBA$_{30}$ monolayer membrane was transferred onto Quantifoil gold grids with a holey carbon support film, having a hole diameter of 0.6 µm (**Figure 3**a).

That the freestanding membrane stretched across the holes could be seen from the TEM images (Figure S6, Supporting Information). However, for high magnification imaging, the Quantifoil grids with holey carbon support were not suitable. Therefore, the grids were sputter-coated with platinum before transferring the membranes (see Figure S6c,d, Supporting Information, for TEM image of a pristine sputter-coated grid). The sputter-coated grid allowed for better imaging of Na_4Ag_{44}-pMBA$_{30}$ monolayer membranes stretched across holey grids (Figure 3b–d; Figure S7, Supporting Information). It is important to note that NCs are inherently electron beam sensitive and, therefore, at higher magnification, beam damage and their aggregation into larger nanoparticles can be observed. The HR-TEM images and IFFT suggests that the monolayer membrane stretched across the hole still incorporated a hexagonal nanocluster assembly (Figure 3d).

AFM measurements showed that the Na_4Ag_{44}-pMBA$_{30}$ monolayer membranes within the holes were smooth and flat (Figure 3e,f). Height profile images indicate that the monolayer membrane drape over the hole (Figure 3g; Figure S8, Supporting Information). Importantly, the height of various 2D membranes deposited on holey support films has been discussed in the literature.[51–55] We used the Quantitative Nanomechanical Measurement-mode of the AFM to obtain the
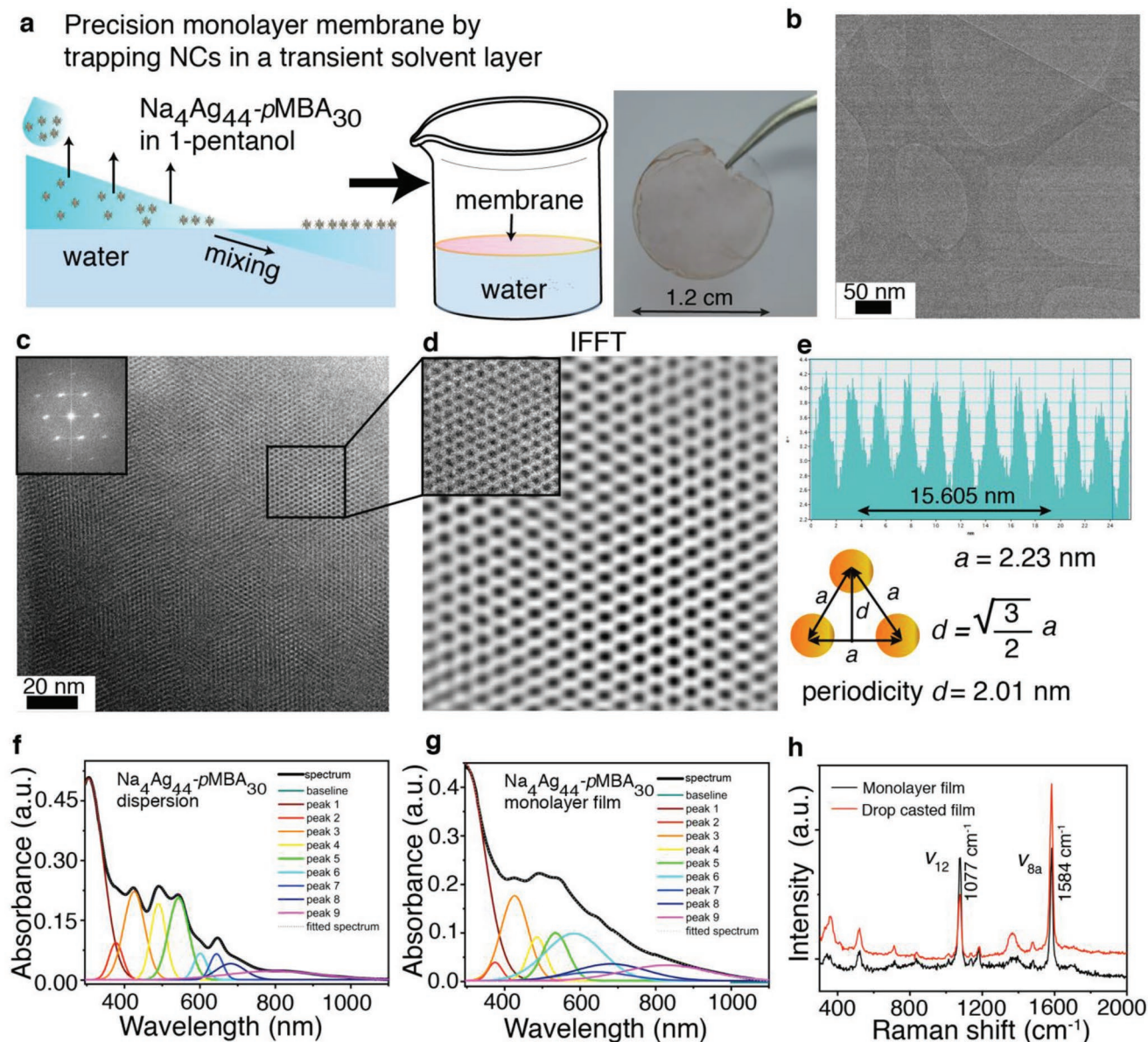
Figure 2. Freestanding Na_4Ag_{44}-pMBA$_{30}$ membranes. a) Schematics showing the formation of the monolayer Na_4Ag_{44}-pMBA$_{30}$ assembly in a liquid-assisted air–water interface method (left). Large area Na_4Ag_{44}-pMBA$_{30}$ monolayer membrane transferred onto a microscope coverslip (right). b) TEM image of the monolayer assembly stretched over a lacey carbon support membrane. c) TEM image suggesting the hexagonal packing of Na_4Ag_{44}-pMBA$_{30}$ NCs (inset shows the FFT). d) IFFT image from the marked area in image c. e) Profile showing the inter-nanoparticle distance and periodicity. f) UV–vis spectrum of Na_4Ag_{44}-pMBA$_{30}$ in aq. dispersion along with peak fitting. g) UV–vis spectrum of Na_4Ag_{44}-pMBA$_{30}$ monolayer membrane. h) Raman spectra of Na_4Ag_{44}-pMBA$_{30}$ monolayer membrane (black) and that of drop-casted Na_4Ag_{44}-pMBA$_{30}$ dispersion (red) showing the presence of the characteristic bands (see Figure S4, Supporting Information).

correct height of the membrane. In this mode, the contact point is evaluated and used as height information which is hence independent of the force applied by the probe. The obtained "real height" images show that the membrane (rather than recessed) is suspended on the rim of the holes whose height is ≈20 nm (see the image of the control grid in Figure S10, Supporting Information).

Next, AFM indentation experiments were carried out on freestanding monolayer membranes suspended on grids having a hole radius of 0.6 µm. For the characterization of the

membrane elasticity, force curves were recorded at the center of the holes. A typical trace of the force–displacement curve is presented in **Figure 4**b. For each sample, several holes covered with the membrane were probed. We observed consistent force–displacement curves for multiple indents on a single spot without breaking the membrane. An increasing force starting from 10 nN was applied until the value of ≈16–18 nN was reached, which represents the maximum load that the suspended membrane can withstand before breaking (Figure S11, Supporting Information, for additional force–displacement
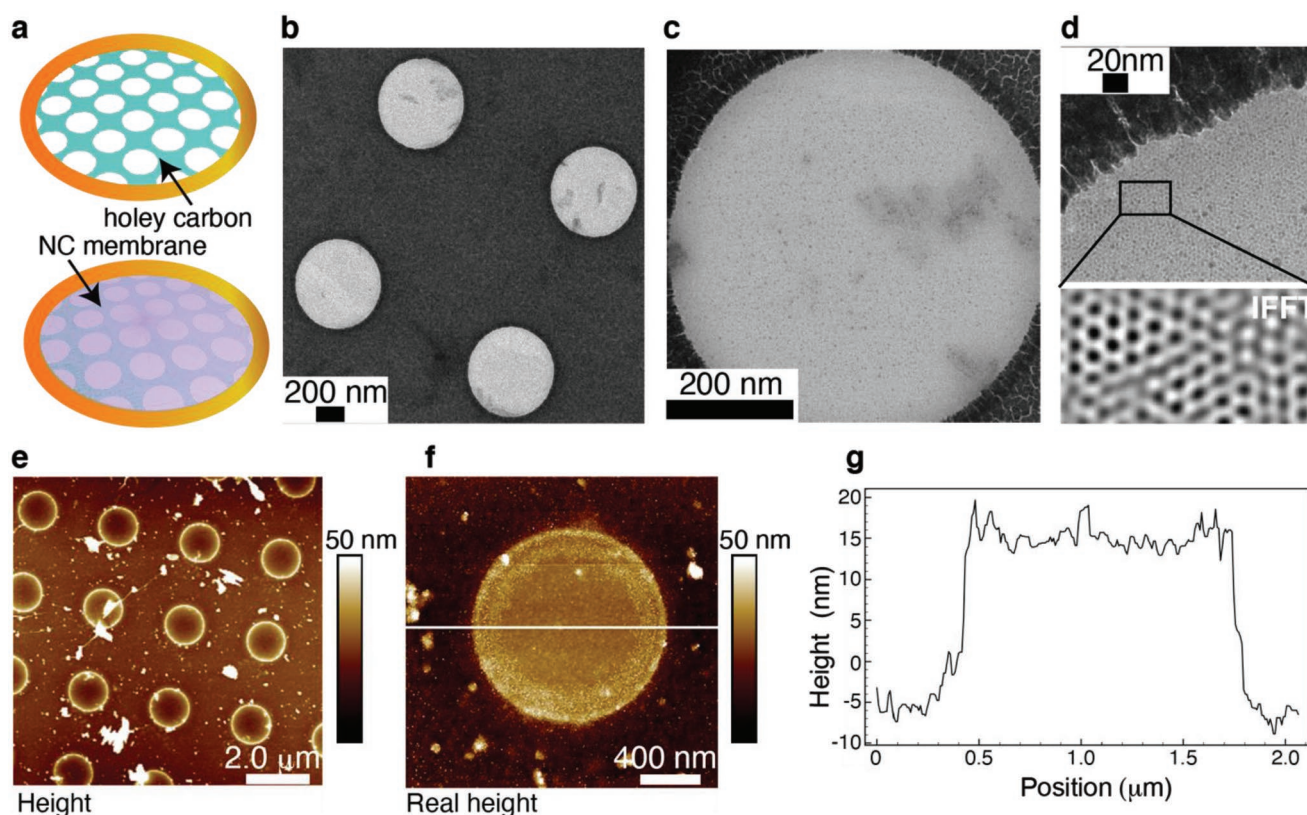
Figure 3. TEM and AFM imaging of Na_4Ag_{44}-pMBA$_{30}$ membranes. a) Schematics showing the deposition of Na_4Ag_{44}-pMBA$_{30}$ membrane on a gold grid with a holey carbon support membrane. b) TEM image showing cluster monolayers spanned across the holes (Figure S5, Supporting Information, for additional images). c) TEM image of one of the holes showing the cluster membrane being present across the hole. d) High-magnification TEM image and IFFT of the marked area showing hcp array of Na_4Ag_{44}-pMBA$_{30}$ (note: NCs are sensitive to electron beam). e) Large area AFM height image of the cluster monolayer deposited on a TEM grid. f,g) AFM image of one of the holes, showing the cluster membrane spanned across the hole, and the corresponding height profile.

curves over different covered holes). Figure 4c,d shows the membrane before and after breakage upon a series of indents, respectively. As expected, the higher is the load applied, the deeper is the penetration depth (Figure 4e; Figures S11 and S12, Supporting Information, for additional AFM images and overlap of multiple $F\delta$ curves, respectively). For small indentations, δ, all curves are linear in force, F. However, when δ considerably exceeds the membrane thickness, h, they turn nonlinear/cubic ($F \approx \delta^3$). At large indentation, the obtained cubic term dominates, allowing to extract Young's modulus, E.[31,56] This is an essential point for the determination of E (see Equation (1)) since the apparent spring constant, k, for small δ, depends on the prestretch of the membrane that is a priori unknown and cannot be used to determine E at small indentations. However, the prestretching of the monolayer membranes can be neglected for larger indentations, where the stretching energy dominates.

For homogeneous membranes, the effective E can be extracted using Equation (1), by analyzing the force curves within the framework of elasticity theory[57,58]

$$F = k\delta + \frac{\pi E h}{3R^2}\delta^3 \qquad (1)$$

where h is the membrane thickness, R is the hole radius, δ is the indentation depth, and k is the spring constant that depends on the prestrain of the membrane and used as a fitting parameter.

The model is applicable for $\delta/h \gg 1$ and a point-like force. This is the case if the tip diameter is small compared to the hole radius, which is valid only for sharp styluses. The Scanasyst tip used in our measurements has a nominal radius of curvature of 2 nm (maximum nominal value at 12 nm). The tip radius was also estimated by tip qualification measurement and revealed a value of ≈11 nm, which closely matches the maximum nominal value and is much smaller than the hole radius. The E values extracted by the fit of the $F(\delta)$ curves, fall in the range between 10 and 30 GPa as shown in the histograms of Figure 4g with Gaussian distribution centered at 14.5 ± 0.2 GPa. The absence of hysteresis between the loading/unloading curves confirms the elastic nature of the Na_4Ag_{44}-pMBA$_{30}$ monolayer membrane. At higher applied loads, however, when the membrane is close to the rupture, sometimes a slight hysteretic behavior is observed, indicating probably that the membrane is damaged or stretched irreversibly beyond a yield point, as also reflected by the low prestress values associated. The calculated average values for Young's modulus of Na_4Ag_{44}-pMBA$_{30}$ membranes fall slightly above the range observed for deformations of
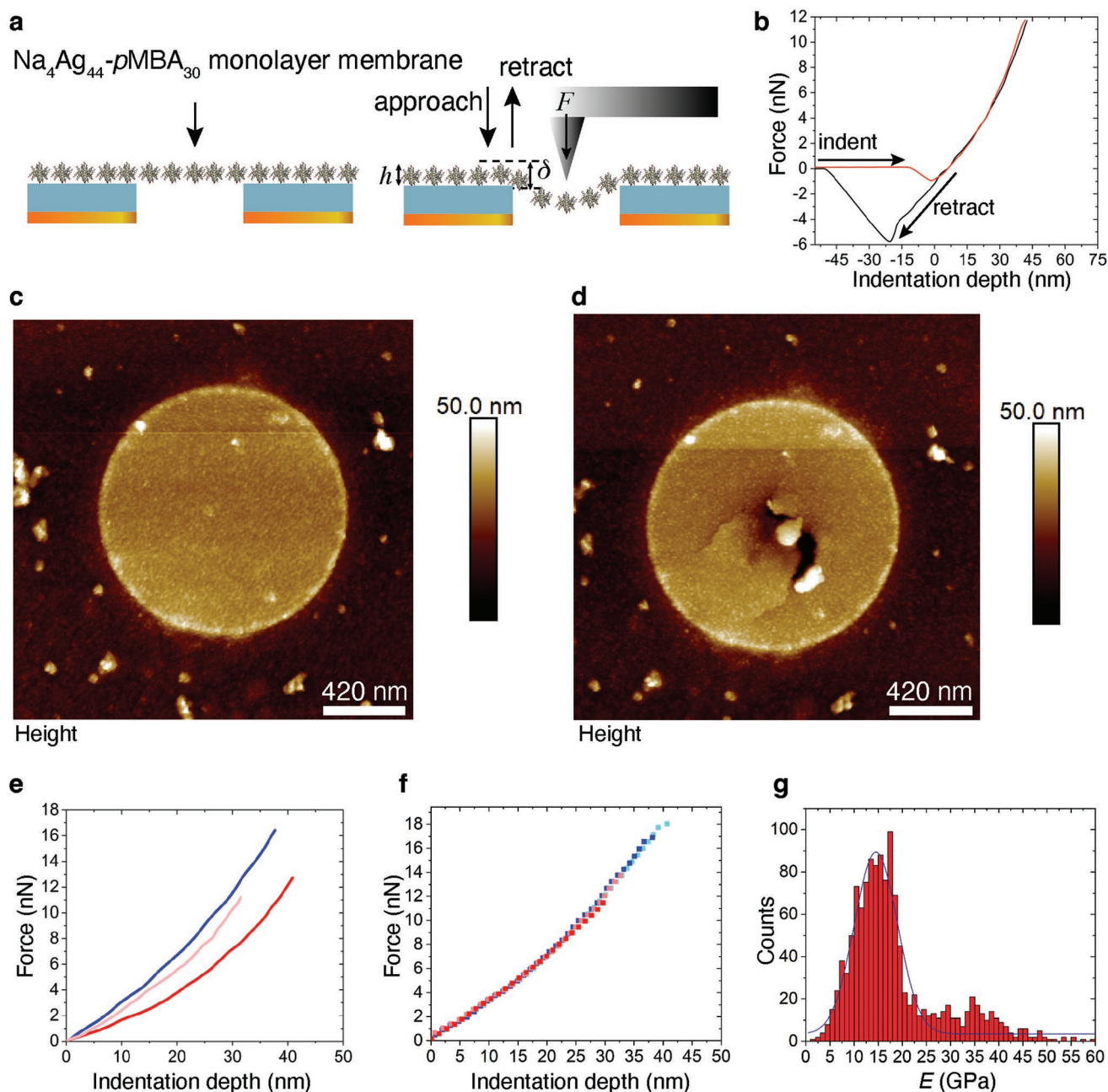
Figure 4. AFM measurements. a) A cartoon representation of the membrane deposited on top of the TEM grid and related AFM experimental setup. b) A typical force–displacement curve and the absence of hysteresis suggests the elastic nature of the membrane. c) AFM height image of the membrane before indentation. d) AFM image of the membrane after many indentation cycles at different close spots. e) Overlap of $F(\delta)$ curves recorded on three different holes covered with membrane. f) $F(\delta)$ curves recorded on the same spot of a hole covered with membrane by increasing force. g) Histogram reporting the E modulus value extracted by fitting the $F(\delta)$ curves.

several larger nanoparticle-based membranes,[31,32,54,59] yet, the distribution of the obtained values is much narrower than the wide distribution range (3–39 GPa) of gold nanoparticle membranes reported earlier.[31]

The high modulus of Na_4Ag_{44}-pMBA$_{30}$ membranes can be attributed to the well-defined H-bonded connectivity of nanoparticles and their structural integrity. In contrast to the narrow size dispersed alkanethiol-capped plasmonic nanoparticle

membranes,[29] the Na_4Ag_{44}-pMBA$_{30}$ clusters are atomically precise with covalently bound short and rigid ligands. Therefore, the Na_4Ag_{44}-pMBA$_{30}$ membranes are devoid of ligand entanglement, a common feature in polymer membranes. Importantly, the solid state structure of Na_4Ag_{44}-pMBA$_{30}$ shows highly directional H-bonding distances between O···H is 1.54 and 2.6 Å for the O···O, and with the angle ∠OHO of 177°.[43,44]

ADVANCED
SCIENCE NEWS

www.advancedsciencenews.com

NANO · MICRO
small

www.small-journal.com

2.4. Surfaced Enhanced Raman Spectroscopy

Noble metal nanoparticles deposited on functionalized surfaces have been studied in the literature as SERS substrate for detection and monitoring antibiotics.[60] Plasmonically coupled metallic nanostructures with ultrasmall ($\approx$1 nm or smaller) nanogaps can generate very strong and tunable electromagnetic fields that result in strong SERS signals from Raman dyes in the gap. However, even small changes (<1 nm) in the structure of the coupled plasmonic nanogaps can significantly affect the localization of electrons and thereby, signal intensity in such plasmonically fabricated metamaterials.[61] High-yield synthetic strategies with nanometer-level structural control and reproducibility are greatly challenging owing to the inherent polydispersity in the size of nanoparticles. While the existing methods utilize highly sophisticated fabrication methods, we show that the Na_4Ag_{44}-pMBA$_{30}$ membranes can overcome some of these challenges. Notably, the membrane can be readily transferred to the substrate and require no surface pretreatment to detect the target Raman-active molecules such as amphotericin B (Amp B, see Supporting Information for details). The Raman spectrum of standard Amp B shows the specific bands at 1559 cm^{-1} corresponding to the C=C stretch due to the hydrophobic polyene domain and at 1157 cm^{-1}, corresponding to the C—C stretching.[62,63] As shown in **Figure 5**a, when Amp B (250 μg mL^{-1}) was drop-casted on Na_4Ag_{44}-pMBA$_{30}$ film, the peak at 1157 cm^{-1} emerged.

Besides, the peak at 1429 cm^{-1} due to the stretching of —COO in Na_4Ag_{44}-pMBA$_{30}$ film suffered a significant blue shift. These spectral features are highly reproducible, as shown using multiple membranes (Figure S14b, Supporting Information). Amp B has been detected before using AgNP as the plasmonic entity.[63] Here, we show that Na_4Ag_{44}-pMBA$_{30}$ films can detect as low as 2.5 μg mL^{-1} of Amp B. Whereas, at this concentration, the characteristic peak was not observed in the case of a similar film containing polydispersed AgNPs (Figure S14d, Supporting Information). Thus, as a proof of concept, it is shown that the precision film made of Na_4Ag_{44}-pMBA$_{30}$ assemblies is more efficient SERS substrate as compared to traditionally used AgNPs.

3. Conclusions

Here we showed self-assembly of atomically precise Na_4Ag_{44}-pMBA$_{30}$ NCs into freestanding elastic membranes with long-range hexagonal intralayer structure over cm^2-scale. This was accomplished by utilizing the hydrogen bonding dimerizations between the terminal p-mercaptobenzoic acid protecting ligands of the neighboring NCs. The patchy distribution of ligands around the metal core directed preferentially intralayer hexagonal assembly (in the ab-plane) and only to a lesser amount interplane hydrogen bonds (in the c-direction). Thereby the lateral growth perpendicular to the layers could be limited upon trapping the clusters in a transient solvent layer on the air–water interface facilitating a long-range intralayer structure within the monolayer. TEM imaging indicates an extended hexagonal 2D packing of the Na_4Ag_{44}-pMBA$_{30}$ NCs in the membrane with a cluster-to-cluster distance of 2.33 nm. This agrees with the triclinic unit cell parameters a and b in the 3D Na_4Ag_{44}-pMBA$_{30}$ X-ray single crystal structure. The membranes could easily be transferred onto various substrates for desired applications. This is an important asset as well-defined colloidal structures have often been achieved upon templating with a specific substrate. On the other hand, the shown freestanding membranes with long-range order are expected to be relevant in applications to combine the mechanical and optoelectronic properties. The membranes behave elastically without any observable hysteresis, and display high Young's modulus of 14.5 $\pm$ 0.2 GPa (based on the Gaussian distribution center resulting from a set of experiments). Finally, the distinct constituent nanocluster spectral peaks remain observable in the membranes, even if slightly broadened, therefore indicating that the intrinsic properties of the individual NCs are retained in self-assembled membranes. These findings suggest that 2D colloidal materials where ligand capped NCs are bound together by H-bonds could raise unique elasticity and stiffness values, also suggesting to combine with optoelectric properties of the nanoclusters for future single-electron transistors, metamaterials, and multifunctional devices.
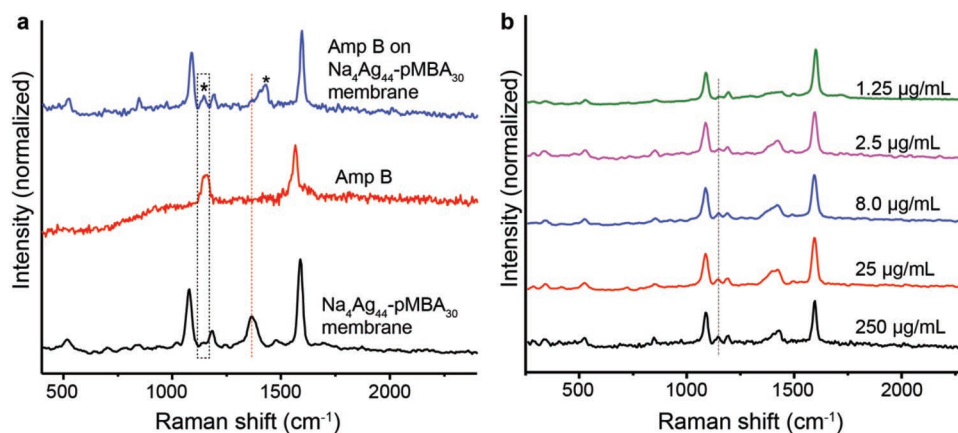

Figure 5. Surface enhanced Raman spectroscopy (SERS) measurements. a) Raman spectra of Na_4Ag_{44}-pMBA$_{30}$ membrane, Amp B, and Amp B (250 μg mL^{-1}) deposited over Na_4Ag_{44}-pMBA$_{30}$ membrane. b) Variable concentration SERS spectra of Amp B deposited on Na_4Ag_{44}-pMBA$_{30}$ membrane.

**ADVANCED
SCIENCE NEWS**

www.advancedsciencenews.com

**NANO · MICRO
small**

www.small-journal.com

Supporting Information

Acknowledgements

Conflict of Interest

The authors declare no conflict of interest.

Author Contributions

A.S., A.G., and I.C. contributed equally to this work. A.S, I.C., and N. conceived and carried out the synthesis and characterization. A.S. and N. carried out self-assembly, electron microscopy imaging, ESI mass spectrometry, and Raman spectroscopy measurements. A.G. conceived and carried out the AFM measurements and analyzed the data together with H.H., K.J., and P.L. T.P., O.I., and N. directed the experimental research. B.M. and A.C. performed the synthesis of NCs and membranes for SERS measurements. All authors contributed to preparation of the final manuscript.

Data Availability Statement

The data that support the findings of this study are available from the corresponding author upon reasonable request.

Keywords

[1] K. S. Novoselov, A. K. Geim, S. V. Morozov, D. Jiang, Y. Zhang, S. V. Dubonos, I. V. Grigorieva, A. A. Firsov, *Science* **2004**, *306*, 666.
[2] X. Peng, L. Peng, C. Wu, Y. Xie, *Chem. Soc. Rev.* **2014**, *43*, 3303.
[3] L. Chen, J. Wen, P. Zhang, B. Yu, C. Chen, T. Ma, X. Lu, S. H. Kim, L. Qian, *Nat. Commun.* **2018**, *9*, 1542.
[4] D. Akinwande, N. Petrone, J. Hone, *Nat. Commun.* **2014**, *5*, 5678.
[5] M. Chhowalla, H. S. Shin, G. Eda, L.-J. Li, K. P. Loh, H. Zhang, *Nat. Chem.* **2013**, *5*, 263.
[6] M. Naguib, V. N. Mochalin, M. W. Barsoum, Y. Gogotsi, *Adv. Mater.* **2014**, *26*, 992.
[7] L. H. Li, Y. Chen, *Adv. Funct. Mater.* **2016**, *26*, 2594.
[8] S. Rosenfeldt, M. Stöter, M. Schlenk, T. Martin, R. Q. Albuquerque, S. Förster, J. Breu, *Langmuir* **2016**, *32*, 10582.
[9] J. N. Coleman, M. Lotya, A. O'Neill, S. D. Bergin, P. J. King, *Science* **2011**, *331*, 568.
[10] J. M. Wofford, S. Nakhaie, T. Krause, X. Liu, M. Ramsteiner, M. Hanke, H. Riechert, J. M. J. Lopes, *Sci. Rep.* **2017**, *7*, 43644.
[11] A. Narita, X.-Y. Wang, X. Feng, K. Müllen, *Chem. Soc. Rev.* **2015**, *44*, 6616.
[12] Q. H. Wang, K. Kalantar-Zadeh, A. Kis, J. N. Coleman, M. S. Strano, *Nat. Nanotechnol.* **2012**, *7*, 699.
[13] F. Xia, H. Wang, D. Xia, M. Dubey, A. Ramasubramanian, *Nat. Photonics* **2014**, *8*, 899.
[14] W. Cheng, N. Park, M. T. Walter, M. R. Hartman, D. Luo, *Nat. Nanotechnol.* **2008**, *3*, 682.
[15] T. Wen, S. A. Majetich, *ACS Nano* **2011**, *5*, 8868.
[16] C. Yu, X. Guo, M. Muzzio, C. T. Seto, S. Sun, *ChemPhysChem* **2019**, *20*, 23.
[17] W. J. Cho, Y. Kim, J. K. Kim, *ACS Nano* **2012**, *6*, 249.
[18] R. Sardar, A. M. Funston, P. Mulvaney, R. W. Murray, *Langmuir* **2009**, *25*, 13840.
[19] S. Zhang, G. Leem, L. Srisombat, T. R. Lee, *J. Am. Chem. Soc.* **2008**, *130*, 113.
[20] C. S. Weisbecker, M. V. Merritt, G. M. Whitesides, *Langmuir* **1996**, *12*, 3763.
[21] V. N. Manoharan, *Science* **2015**, *349*, 1253751.
[22] K. E. B. Doncom, L. D. Blackman, D. B. Wright, M. I. Gibson, R. O'Reilly, *Chem. Soc. Rev.* **2017**, *46*, 4119.
[23] T. J. Woehl, T. Prozorov, *J. Phys. Chem. C* **2015**, *119*, 21261.
[24] T. P. Bignioni, X.-M. Lin, T. T. Nguyen, E. I. Crowin, T. A. Witten, H. M. Jaeger, *Nat. Mater.* **2006**, *5*, 265.
[25] A. Desireddy, C. P. Joshi, M. Sestak, S. Little, S. Kumar, N. J. Podraza, S. Massilac, R. W. Collins, T. P. Bigioni, *Thin Solid Films* **2011**, *519*, 6077.
[26] A. Dong, J. Chen, P. M. Vora, J. M. Kikkawa, C. B. Murray, *Nature* **2010**, *266*, 474.
[27] J. Pang, S. Xiong, F. Jaeckel, Z. Sun, D. Dunphy, C. J. Brinker, *J. Am. Chem. Soc.* **2008**, *130*, 3284.
[28] C. Klinke, *Europhys. Lett.* **2017**, *119*, 36002.
[29] K. E. Mueggenburg, X.-X. Lin, R. H. Goldsmith, H. M. Jaeger, *Nat. Mater.* **2007**, *6*, 656.
[30] A. Raveendran, M.-V. Meli, *ACS Omega* **2017**, *2*, 4411.
[31] W. Cheng, M. J. Campolongo, J. J. Cha, S. J. Tan, C. C. Umbach, D. A. Muller, D. Luo, *Nat. Mater.* **2009**, *8*, 519.
[32] a) F. Alibart, S. Pleutin, D. Guérin, C. Novembre, S. Lenfant, K. Lmimouni, C. Gamrat, D. Vuillaume, *Adv. Funct. Mater.* **2010**, *22*, 330; b) F. Alibert, S. Pleutin, O. Bichler, C. Gamrat, T. Serrano-Gotarrendona, B. Linares-Barranco, D. Vuillaume, *Adv. Funct. Mater.* **2012**, *8*, 609.
[33] J. Langer, D. J. de Aberasturi, J. Aizpurua, R. A. Alvarez-Puebla, B. Auguié, J. J. Baumberg, G. C. Bazan, S. E. J. Bell, A. Boisen, A. G. Brolo, J. Choo, D. Cialla-May, V. Deckert, L. Fabris, K. Faulds, F. J. G. de Abajo, R. Goodacre, D. Graham, A. J. Haes, C. L. Haynes, C. Huck, T. Itoh, M. Käll, J. Kneipp, N. A. Kotov, H. Kuang, E. C. L. Ru, H. K. Lee, J.-F. Li, X. Y. Ling, et al., *ACS Nano* **2020**, *14*, 28.
[34] P. Pal, A. Bonyar, M. Veres, L. Himics, L. Balazs, L. Juhasz, I. A. Csarnovics, *Sens. Actuators, A* **2020**, *314*, 112225.
[35] R. X. He, R. Liang, P. Peng, *J. Nanopart. Res.* **2017**, *19*, 267.
[36] a) I. Chakraborty, T. Pradeep, *Chem. Rev.* **2017**, *117*, 8208; b) R. Jin, C. Zeng, M. Zhou, Y. Chen, *Chem. Rev.* **2016**, *116*, 10346; c) H. Häkkinen, *Nat. Chem.* **2012**, *4*, 443.

[37] a) Y. Li, M. Zhoud, R. Jin, *Adv. Mater.* **2021**, *33*, 2006591; b) B. Zhang, J. Chen, Y. Cao, O. J. H. Chai, J. Xie, *Small* **2021**, *17*, 2004381.

[38] a) T. Kawawaki, A. Ebina, Y. Hosokawa, S. Ozaki, D. Suzuki, S. Hossain, Y. Negishi, *Small* **2021**, *17*, 2005328; b) F. Gao, Q. Yuan, P. Cai, L. Gao, L. Zhao, M. Liu, Y. Yao, Z. Chai, X. Gao, *Adv. Sci.* **2019**, *6*, 1801671; c) L. Gao, Y. Zhang, L. Zhao, W. Niu, Y. Tang, F. Gao, P. Cai, Q. Yuan, X. Wang, H. Jiang, X. Gao, *Sci. Adv.* **2020**, *6*, 1421.

[39] a) S. Chandra, Nonappa, G. Beaune, A. Som, S. Zhou, J. Lahtinen, H. Jiang, J. V. I. Timonen, O. Ikkala, R. H. A. Ras, *Adv. Opt. Mater.* **2019**, *7*, 1900620; b) J. V. Rival, P. Mymoona, K. M. Lakshmi, Nonappa, T. Pradeep, E. Shibu, *Small* **2021**, *17*, 2005718; c) V. Hynninen, S. Chandra, S. Das, M. Amini, Y. Dai, S. Lepikko, P. Mohammadi, S. Hietala, R. H. A. Ras, Z. Sun, O. Ikkala, Nonappa, *Small* **2021**, *17*, 2005205; d) A. Chakraborty, H. Dave, B. Mondal, Nonappa, E. Khatun, T. Pradeep, *J. Phys. Chem. B* **2022**, *126*, 1842.

[40] Nonappa, T. Lahtinen, J. S. Haataja, T.-R. Tero, H. Häkkinen, O. Ikkala, *Angew. Chem., Int. Ed.* **2016**, *55*, 16035.

[41] Nonappa, O. Ikkala, *Adv. Funct. Mater.* **2018**, *28*, 1704328.

[42] A. Som, I. Chakraborty, T. A. Maark, S. Bhat, T. Pradeep, *Adv. Mater.* **2016**, *28*, 2827.

[43] A. Chakraborty, A. C. Fernandez, A. Som, B. Mondal, G. Natarajan, G. Paramasivam, T. Lahtinen, H. Häkkinen, Nonappa, T. Pradeep, *Angew. Chem., Int. Ed.* **2018**, *57*, 6522.

[44] Z. Wu, C. Dong, Y. Li, H. Hao, H. Zhang, Z. Lu, B. Yang, *Angew. Chem., Int. Ed.* **2013**, *52*, 9952.

[45] A. Desireddy, B. E. Conn, J. Guo, B. Yoon, R. N. Barnett, B. M. Monahan, K. Kirschbaum, W. P. Griffith, R. L. Whetten, U. Landman, T. P. Bigioni, *Nature* **2013**, *501*, 399.

[46] B. Yoon, W. D. Luedtke, R. N. Barnett, J. Gao, A. Desireddy, B. E. Conn, T. P. Bigioni, U. Landman, *Nat. Mater.* **2014**, *13*, 807.

[47] J. Zasadzinski, R. Viswanathan, L. Madsen, J. Garnaes, D. K. Schwartz, *Science* **1994**, *263*, 1726.

[48] K. Ariga, Y. Yamauchi, T. Mori, J. P. Hill, *Adv. Mater.* **2013**, *25*, 6477.

[49] a) D. H. McCullough, S. L. Regen, *Chem. Commun.* **2004**, 2787; b) K. Ariga, *Langmuir* **2020**, *36*, 7158.

[50] a) G. Palazzo, L. Carbone, G. Colafemmina, R. Angelico, A. Ceglieb, M. Giustini, *Phys. Chem. Chem. Phys.* **2004**, *6*, 1423; b) H. You, Y. Ji, L. Wang, S. Yang, Z. Yang, J. Fang, X. Song, B. Ding, *J. Mater. Chem.* **2012**, *22*, 1998.

[51] A. Lipatov, H. Lu, M. Alhabeb, B. Anasori, A. Gruverman, Y. Gogotsi, A. Sinitskii, *Sci. Adv.* **2018**, *4*, 0491.

[52] R. Zhang, V. Koutsos, R. Cheung, *Appl. Phys. Lett.* **2016**, *108*, 042104.

[53] A. Zandiatashbar, G.-H. Lee, S.-J. An, S. Lee, N. Mathew, M. Terrones, T. Hayashi, C. R. Picu, J. Hone, N. Koratkar, *Nat. Commun.* **2014**, *5*, 3186.

[54] C. Lee, X. Wei, J. W. Kysar, J. Hone, *Science* **2008**, *321*, 385.

[55] J. He, P. Kanjanaboos, N. L. Frazer, A. Weis, X.-M. Lin, H. M. Jaeger, *Small* **2010**, *6*, 1449.

[56] M. Kocun, W. Mueller, M. Maskos, I. Mey, B. Geil, C. Steinemd, A. Janshoff, *Soft Matter* **2010**, *6*, 2508.

[57] U. Komaragiri, M. R. Begley, J. G. Simmonds, *J. Appl. Mech.* **2005**, *72*, 203.

[58] K. Tak, W. Shu, G. David, A. Dillard, *Thin Solid Films* **2003**, *425*, 150.

[59] Y. Wang, H. Chan, B. Narayanan, S. P. McBride, S. K. R. Sankaranarayanan, S. X.-M. Lin, H. M. Jaeger, *ACS Nano* **2017**, *11*, 8026.

[60] S. J. Clarke, R. E. Littleford, W. E. Smith, R. Goodacre, *Analyst* **2005**, *130*, 1019.

[61] J.-M. Nam, J.-W. Oh, H. Lee, Y. D. Suh, *Acc. Chem. Res.* **2016**, *49*, 2746.

[62] R. Miyaoka, M. Hosokawa, M. Ando, T. Mori, H. Hamaguchi, H. Takeyama, *Mar. Drugs* **2014**, *12*, 2827.

[63] W. V. La Via, J. L. Lambert, M. J. Pelletier, J. M. Morookian, S. J. Sirk, D. Mickiene, T. J. Walsh, M. S. Borchert, *Med. Mycol.* **2006**, *44*, 169.